Compressed-Domain Detection and Estimation for Colocated MIMO Radar

EHSAN TOHIDI [ID], Member, IEEE
Eurecom, Biot, France

ALIREZA HARIRI
HAMID BEHROOZI [ID], Member, IEEE
MOHAMMAD MAHDI NAYEBI, Senior Member, IEEE
Sharif University of Technology, Tehran, Iran

GEERT LEUS [ID], Fellow, IEEE
Delft University of Technology, Delft, The Netherlands

ATHINA P. PETROPULU [ID], Fellow, IEEE
Rutgers—The State University of New Jersey, New Brunswick USA

This article proposes a compressed-domain signal processing (CSP) multiple-input multiple-output (MIMO) radar, a MIMO radar approach that achieves substantial sample complexity reduction by exploiting the idea of CSP. CSP MIMO radar involves two levels of data compression followed by target detection at the compressed domain. First, compressive sensing is applied at the receive antennas, followed by a Capon beamformer, which is designed to suppress clutter. Exploiting the sparse nature of the beamformer output, a second compression is applied to the filtered data. Target detection is subsequently conducted by formulating and solving a hypothesis testing problem at each grid point of the discretized angle space. The proposed approach enables an eightfold reduction of the sample complexity in some settings as compared to a conventional compressed sensing (CS) MIMO radar, thus enabling faster target detection. Receiver operating characteristic curves of the proposed detector are provided. Simulation results show that the proposed approach outperforms recovery-based CS algorithms.

I. INTRODUCTION

The emergence of a multiple-input multiple-output (MIMO) radar opened up a wide research area, promising the same resolution as phased array technology but with significantly fewer antennas elements, or higher resolution with the same number of antennas. MIMO radar transmit different waveforms from their antennas. Based on antennas distances, a MIMO radar is categorized into widely separated and colocated. Large distances among antennas in a widely separated MIMO radar cause different transmitter–receiver pairs to look at a target from different angles; this provides spatial diversity and results in high-resolution target localization and enhanced target detection and estimation [1]–[3]. In the colocated MIMO radar, exploiting waveform diversity results in flexible beampattern design and improved angular resolution [4]–[7]. In this article, we focus on the colocated MIMO radar. Despite many advantages, the requirement for a large amount of data and associated computational complexity are viewed as the main drawbacks of the MIMO radar [8], [9]. Fortunately, due to the low number of targets in the target space (angle, range, and speed), the target echoes are sparse [10]–[15]. This characteristic enables the incorporation of compressed sensing (CS) theory, which, under certain conditions, allows for lower than Nyquist rate sampling with a negligible performance reduction [16], [17]. A general discussion of CS applied to radar can be found in [10] and [18]. MIMO radar's ability to achieve high angle resolution with small numbers of elements renders them indispensable for automotive applications. This advantage has been exploited by almost all major automotive Tier-1 suppliers in their different types of radar products, such as short-range radar, medium-range radar, and long-range radar [19]–[22].

CS application to MIMO radar has received a lot of attention recently, e.g., [9], [23]–[31]. For instance, target detection and localization in the MIMO radar using CS is discussed in [25] and [26], while improving angular resolution with a lower number of elements in a colocated MIMO radar is studied in [9], [23], and [27]. Similarly, power allocation and waveform design in CS MIMO radar is investigated in [24] and [28]. In all aforementioned works, the signal used for detection and/or estimation is first reconstructed by using a general-purpose CS recovery algorithm such as orthogonal matching pursuit (OMP) [25], basis pursuit denoising or compressive sampling matching pursuit [32], alternating direction method of multipliers [26], or problem-specific algorithms [33], [34]. In the cited methods, CS is used to reduce the amount of data collected and transmitted to a fusion center, where sparse signal recovery is carried out. However, recovering the sparse signal switches the problem back to the high rate domain and, thus, does not take full advantage of the CS-enabled reduction of a large amount of data. In many radar applications, the original signal may not be of interest, and the main aim

is to accomplish radar inference tasks (e.g., detection and estimation). Therefore, signal processing in the CS domain (i.e., without reconstruction) is desirable. Note that from an information-theoretic aspect, signal reconstruction does not increase the available information. Furthermore, if the sensing matrix does not have low coherence, the recovery may be incorrect. In this article, we go one step further on the use of the CS idea; we do not recover the underlying sparse signal, but rather perform target detection in the compressed domain, using compressed-domain signal processing (CSP). We show that CSP-based target detection and parameter estimation not only preserves the performance and significantly reduces the number of computations, but also prevents the high flow of data after recovery, which is one of the fundamental motivations of employing CS [35].

CSP has been studied in various applications. For instance, CSP is used in [36] to detect sparse signals in additive white Gaussian noise and estimate the degree of sparsity. Similarly, a CSP-based symbol detector for ultrawideband communications is proposed in [37]. Also, CSP is used in [38] to accomplish joint compressive single target detection and parameter estimation in a radar. Algorithms for solving inference problems, such as detection, classification, estimation, and filtering based on CSP, are proposed in [38], while in [39], the idea of using CSP for space–time adaptive processing is presented. The task of inferring the modulation of a communication signal directly in the compressed domain is considered in [40] and [41]. Furthermore, in [42], a minimum-variance distortionless response (MVDR) beamformer is used in the compressed domain for the task of spectrum sensing. However, clutter is not considered in the signal model, and the performance is only evaluated through simulations.

Clutter is a critical nuisance component in radar signal processing [43], and clutter suppression is a very important task [44]–[47]. Clutter changes the target scene, making it less sparse. Therefore, the performance of CS-based radar detection methods deteriorates in the presence of clutter. The Capon beamformer, also known as the MVDR, is a common clutter suppression approach that relies on the availability of clutter statistics (i.e., the clutter covariance matrix). In the context of CS-based colocated MIMO radar, Yu *et al.* [48] applies Capon beamforming on the compressed clutter contaminated target echoes, before proceeding with CS-based sparse signal recovery. In this article, we consider the same scenario as in [48]. We apply Capon beamforming on the compressed radar returns, but unlike [48], we proceed with target detection by operating directly in the compressed domain.

A. Contributions

The main contribution of this article is a CSP approach for detection and parameter estimation of a noise and clutter contaminated target in a colocated MIMO radar scenario. In particular, we have the following.

- We formulate and solve a hypothesis testing problem by operating in the compressed samples domain.

- We employ a Capon beamformer as a preprocessing step to reduce the clutter power. The beamformer sparsifies the target scene, which allows us to use a second compression at the beamformer output, thus achieving further sample complexity savings.
- Through receiver operating characteristic (ROC) analysis, and also simulations, we illustrate that the CSP MIMO radar performs well achieving an eightfold sample complexity reduction in some settings as compared to recovery-based methods. This translates to faster detection, making the proposed approach a good candidate for low-latency applications, such as automotive radar. Interestingly, in addition to having lower complexity, the proposed approach outperforms recovery-based algorithms in terms of angle estimation accuracy in the case of multiple targets.

B. Outline and Notations

The rest of this article is organized as follows. Section II provides the required preliminaries. The signal model is introduced in Section III. The CSP algorithm is proposed in Section IV. Simulation results are reported in Section V. Finally, Section VI concludes this article.

We adopt the notation of using boldface lowercase for vectors $\boldsymbol{a}$, and bold face uppercase for matrices $\boldsymbol{A}$, where $\boldsymbol{a}_i$ is the ith column of the matrix $\boldsymbol{A}$. The transpose, Hermitian, complex conjugate, and pseudoinverse operators are denoted by the symbols $(.)^T$, $(.)^H$, $(.)^*$, and $(.)^\dagger$, respectively. Given a set of indices $\mathcal{S}$, $\boldsymbol{A}[\mathcal{S}]$ is a matrix composed of the columns of $\boldsymbol{A}$ with indices in the set $\mathcal{S}$. $\mathbb{R}^{N \times M}$ and $\mathbb{C}^{N \times M}$ are the set of $N \times M$ real and complex matrices, respectively. Finally, $\mathrm{diag}(\boldsymbol{A}_1, \ldots, \boldsymbol{A}_N)$ indicates the block diagonal matrix formed by matrices $\boldsymbol{A}_1, \ldots, \boldsymbol{A}_N$ along the main diagonal.

II. SYSTEM MODEL

Consider a colocated MIMO radar with I transmitters and R receivers. We assume that the transmitters and receivers form a uniform linear array with $\lambda/2$ spacing, where λ is the wavelength. The antenna configuration is shown in Fig. 1(a) (similar to the configuration in [49] and [50]). Let $s_i(n)$ denote the discrete-time baseband signal transmitted by the ith transmitter. The transmit steering vector is given by

$$\boldsymbol{a}(\theta) = [\exp(j2\pi f_c \tau_1(\theta)), \ldots, \exp(j2\pi f_c \tau_I(\theta))]^T \quad (1)$$

where $\tau_i(\theta)$, $i = 1, \ldots, I$, is the propagation delay from the ith transmitter to the target at angle θ with respect to the array axis and f_c is the carrier frequency (i.e., $f_c = c/\lambda$, where c is the speed of light). Furthermore, the receive steering vector is

$$\boldsymbol{b}(\theta) = [\exp(j2\pi f_c \tilde{\tau}_1(\theta)), \ldots, \exp(j2\pi f_c \tilde{\tau}_R(\theta))]^T \quad (2)$$

where $\tilde{\tau}_r(\theta)$, $r = 1, \ldots, R$, is the propagation delay from a target at angle θ to the rth receiver. Let us assume that there are Q targets in the region of interest. On sampling the received signals with the Nyquist sampling interval T_s, the
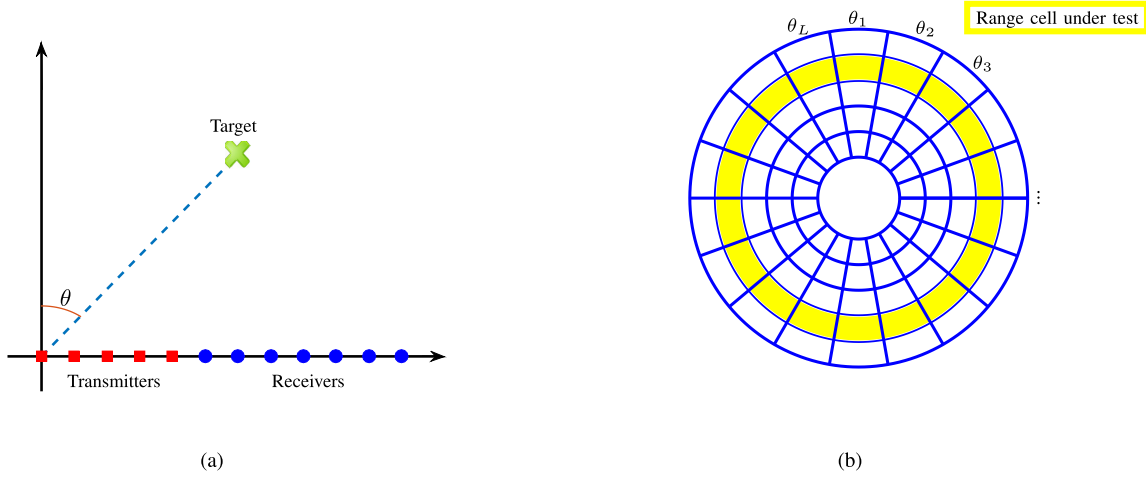
Fig. 1. MIMO radar system model. (a) Configuration of the radar with I transmitters and R receivers placed in a uniform linear array with $\lambda/2$ spacing. (b) All the range and angle cells where a specific range cell (i.e., the colored one) is under test.

obtained samples across all receivers at sampling instance n, i.e., $x_1(n), \ldots, x_R(n)$, can be expressed in a vector form as

$$x(n) = \sum_{q=1}^{Q} \alpha_q b(\theta_q) a^H(\theta_q) s(n) + \epsilon(n), \quad n = 1, \ldots, N \quad (3)$$

where $x(n) = [x_1(n), \ldots, x_R(n)]^T$; $\alpha_q, q = 1, \ldots, Q$, is the complex amplitude of the qth target as seen by the receivers (due to the colocated MIMO radar assumption, the radar cross section of each target seen by all transmitter–receiver pairs is the same). Here, it is assumed that α_qs are constant during the observation interval (i.e., Swerling I model), $s(n) = [s_1(n), \ldots, s_I(n)]^T$ is the nth time sample of the transmit signal vector, and $\epsilon(n)$ is the noise plus clutter term at the receivers. $\epsilon(n)$ is assumed to be complex Gaussian with a covariance matrix $R_N \in \mathbb{C}^{R \times R}$, i.e., $\epsilon(n) \sim \mathcal{CN}(0, R_N)$. Also, we assume that $\alpha_q \sim \mathcal{CN}(0, \sigma_\alpha^2)$ [43]. For simplicity, let us assume that target's angle is the only parameter of interest. Adding velocity to (3) would be addressed in a similar fashion, i.e., it would amount to adding velocity to the hypothesis test and searching in angle-velocity space for both detection and estimation tasks. Also, similar to other works on the target angle of arrival estimation (e.g., [9]), the data vector in (3) is considered for a specific range cell, and therefore, the delay is known and can be compensated [see Fig. 1(b)]. Henceforth, to cover the whole range space, the entire procedure of detection and estimation would have to be performed separately for each range cell.

Suppose the angle space of interest has been discretized into L uniform grid angles $\mathcal{L} = \{\theta_1, \ldots, \theta_L\}$ and the targets lie on the grid. Then, (3) can be reformulated as

$$x(n) = \Psi(n)\beta + \epsilon(n) \quad (4)$$

where $\Psi(n) \in \mathbb{C}^{R \times L}$ is the nth sample of the measurement matrix, in which the lth column, $\psi_l(n)$, is parameterized

based on the grid angle θ_l and equals

$$\psi_l(n) = b(\theta_l) a(\theta_l)^H s(n). \quad (5)$$

Moreover, $\beta \in \mathbb{C}^{L \times 1}$ is the target amplitude vector, determined as

$$\beta_l = \begin{cases} \alpha_q, & \text{if the } q\text{th target is at angle } \theta_l \\ 0, & \text{otherwise.} \end{cases} \quad (6)$$

Stacking the signals of N Nyquist samples obtained by all antennas, the total received data vector is given by

$$x = \begin{bmatrix} \Psi(1) \\ \vdots \\ \Psi(N) \end{bmatrix} \beta + \begin{bmatrix} \epsilon(1) \\ \vdots \\ \epsilon(N) \end{bmatrix} = \Psi\beta + \epsilon \quad (7)$$

where $\Psi \in \mathbb{C}^{RN \times L}$ is the total measurement matrix and ϵ is a complex Gaussian vector with a covariance matrix $\tilde{R}_N \in \mathbb{C}^{RN \times RN}$, i.e., $\epsilon \sim \mathcal{CN}(0, \tilde{R}_N)$.

If there are a small number of targets within the range cell under investigation, β will be sparse [18]. This implies that under certain conditions [18], all information about β is retained in the compressed vector $\bar{x} \in \mathbb{C}^{M_1 \times 1}$, for which it holds that

$$\bar{x} = \Phi_{(1)}\Psi\beta + \Phi_{(1)}\epsilon = \Lambda\beta + \xi \quad (8)$$

where $\Phi_{(1)} \in \mathbb{R}^{M_1 \times RN}$, with $M_1 < RN$ being the compression matrix performing a joint temporal and spatial CS, along the time and array domains, respectively, and we define the first compression ratio $\mathrm{CR}_1 = \frac{RN}{M_1}$ as the ratio of the number of samples in regular sensing, RN, to the number of compressed measurements, M_1. In addition, $\Lambda = \Phi_{(1)}\Psi \in \mathbb{C}^{M_1 \times L}$ and $\xi = \Phi_{(1)}\epsilon \in \mathbb{C}^{M_1 \times 1}$.

In the following, we address the problem of detecting whether a target exists within the grid angles, and if it does, we estimate the target's angle by operating at the compressed sample domain.
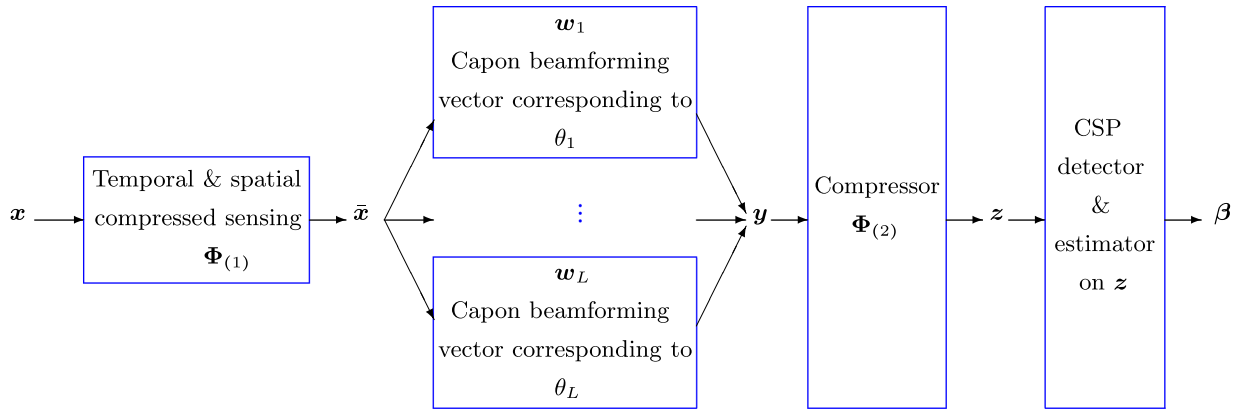
IEEE TRANSACTIONS ON AEROSPACE AND ELECTRONIC SYSTEMS VOL. 56, NO. 6 DECEMBER 2020

Fig. 2. High-level overview of the proposed method.

III. PROPOSED APPROACH

In a practical setting, the received data are contaminated by clutter, which destroys the sparsity of the measured signal $\bar{x}$. Typically, the clutter arises due to reflections by the landscape and thus can be studied when no targets exist. Here, we assume that statistical information about the clutter is available in the form of a clutter covariance matrix. In such case, the Capon's MVDR beamformer [51] can be constructed and applied to the obtained data to reduce clutter and thus make the scene sparser. The objective of Capon's MVDR beamformer is to design a filter so that at the filter output, the noise and clutter power is minimized, while leaving the desired signal without distortion [51]. The Capon weighting vector for each angle cell is obtained by solving the following optimization problem:

$$\min_{\boldsymbol{w}_l} \quad \boldsymbol{w}_l^H \boldsymbol{R}_C \boldsymbol{w}_l$$
$$\text{subject to} \quad \boldsymbol{w}_l^H \boldsymbol{\lambda}_l = 1 \tag{9}$$

where $\boldsymbol{w}_l$ is the weighting vector matched to the lth angle cell and $\boldsymbol{R}_C = \boldsymbol{\Phi}_{(1)} \tilde{\boldsymbol{R}}_N \boldsymbol{\Phi}_{(1)}^T$ is the covariance matrix of the measured clutter and noise, $\boldsymbol{\xi}$. Moreover, $\boldsymbol{\lambda}_l$ is the lth column of $\boldsymbol{\Lambda}$. The optimization problem in (9) has a closed-form solution given by [51]

$$\boldsymbol{w}_l = \frac{\boldsymbol{R}_C^{-1} \boldsymbol{\lambda}_l}{\boldsymbol{\lambda}_l^H \boldsymbol{R}_C^{-1} \boldsymbol{\lambda}_l}. \tag{10}$$

We construct a clutter suppression matrix via concatenating the weighting vectors of all angle cells, i.e., $\boldsymbol{W} = [\boldsymbol{w}_1, \ldots, \boldsymbol{w}_L] \in \mathbb{Z}^{M_1 \times L}$. We then apply the clutter suppression matrix to the compressed measurement vector of (8), obtaining the clutter and noise mitigated data as

$$\boldsymbol{y} = \boldsymbol{W}^H \boldsymbol{\Lambda} \boldsymbol{\beta} + \boldsymbol{W}^H \boldsymbol{\xi} = \boldsymbol{\Theta} \boldsymbol{\beta} + \boldsymbol{v} \tag{11}$$

where $\boldsymbol{\Theta}$ is the dictionary matrix with $\boldsymbol{\theta}_l$ corresponding to the lth angle cell, and $\boldsymbol{v}$ is the clutter and noise residuals after applying the Capon beamformer with covariance matrix $\boldsymbol{R}_T = \boldsymbol{W}^H \boldsymbol{R}_C \boldsymbol{W}$.

REMARK 1 When the radar platform is moving, prior observations can lead to models for clutter and consequently $\boldsymbol{R}_C$.

Our estimate for $\boldsymbol{R}_C$ can also be updated in time, based on the received measurements. More precisely, in applications that the clutter-plus-noise covariance matrix is changing smoothly, we can apply a gradually updating technique such as clutter map on an ordinary covariance matrix estimation method. Since $\boldsymbol{w}_l$ is dependent on the clutter statistics, a change in $\boldsymbol{R}_C$ necessitates the recalculation of $\boldsymbol{w}_l$. However, based on the way that $\boldsymbol{R}_C$ is changing, it might be possible to update its inverse using the matrix inversion lemma and therefore recalculate $\boldsymbol{w}_l$ with a low computational complexity method. In this article, the analysis and simulations are provided for a static case (i.e., one snapshot), while a thorough analysis is required to study a dynamic scenario.

The spare nature of the Capon beamformer output allows us to achieve further sample reduction by employing another compression matrix $\boldsymbol{\Phi}_{(2)} \in \mathbb{R}^{M_2 \times L}$ as follows [48]:

$$\boldsymbol{z} = \boldsymbol{\Phi}_{(2)} \boldsymbol{\Theta} \boldsymbol{\beta} + \boldsymbol{\Phi}_{(2)} \boldsymbol{v} \tag{12}$$

where $\text{CR}_2 = \frac{L}{M_2}$ is the second compression ratio.

The main problem is now reformulated as determining $\boldsymbol{\beta}$ based on the data vector $\boldsymbol{z}$ containing the nuisance term $\boldsymbol{\Phi}_{(2)} \boldsymbol{v}$ (see Fig. 2). Since we just consider a single range cell, we can restrict our attention to scenarios with a low number of targets. First, we present the single-target scenario, propose detection and angle estimation algorithms, and provide mathematical analytics for the ROC of the proposed detector. Then, we proceed to the more realistic multitarget scenario. We subsequently discuss the interrelation of single- and multitarget scenarios, in order to properly extend the proposed single-target algorithm based on such a relationship.

A. Single-Target Scenario

In this part, we restrict our attention to the single-target case, i.e., $Q = 1$. We can write the hypothesis test based on the data vector in the following form:

$$\boldsymbol{z} = \begin{cases} \boldsymbol{\Phi}_{(2)}(\alpha \boldsymbol{\theta}_t + \boldsymbol{v}), & \mathcal{H}_1 : \text{if a target exists} \\ \boldsymbol{\Phi}_{(2)} \boldsymbol{v}, & \mathcal{H}_0 : \text{otherwise} \end{cases} \tag{13}$$

where α and $t \in \{1, \ldots, L\}$ are the unknown target's amplitude and index of angle cell, respectively. If a target exists, its angle cell is not known *a priori*; hence, the usual likelihood ratio test (LRT) cannot be computed and used for detection. Instead, we will use the generalized likelihood ratio test (GLRT), in which the LRT is maximized over all grid angles to find the optimum angle cell. The LRT value at the optimal point should then be compared with a proper threshold to test if a target exists or not.

To determine the threshold, in the following, we compute the probability density function (PDF) of the compressed measurement vector for the two hypotheses. Since $\boldsymbol{v}$ has a complex Gaussian distribution with covariance matrix $\boldsymbol{R}_T$, conditioned on $\mathcal{H}_0$, $\boldsymbol{z}$ is a vector with distribution $\mathcal{CN}(0, \boldsymbol{\Phi}_{(2)}\boldsymbol{R}_T\boldsymbol{\Phi}_{(2)}^T)$. Thus, for the null hypothesis, we have [52, p. 258]

$$f(\boldsymbol{z}|\mathcal{H}_0) = \frac{1}{\pi^{M_2}|\boldsymbol{A}|}\exp\left(-\boldsymbol{z}^H\boldsymbol{A}^{-1}\boldsymbol{z}\right) \qquad (14)$$

where

$$\boldsymbol{A} = \boldsymbol{\Phi}_{(2)}\boldsymbol{R}_T\boldsymbol{\Phi}_{(2)}^T. \qquad (15)$$

For hypothesis $\mathcal{H}_1$, the PDF of $\boldsymbol{z}$ conditioned on α and t is given by

$$f(\boldsymbol{z}|\mathcal{H}_1, \alpha, t) = \mathcal{CN}(\alpha\boldsymbol{\Phi}_{(2)}\boldsymbol{\theta}_t, \boldsymbol{A})$$
$$= \frac{1}{\pi^{M_2}|\boldsymbol{A}|}\exp(-(\boldsymbol{z} - \alpha\boldsymbol{\Phi}_{(2)}\boldsymbol{\theta}_t)^H$$
$$\boldsymbol{A}^{-1}(\boldsymbol{z} - \alpha\boldsymbol{\Phi}_{(2)}\boldsymbol{\theta}_t)) \qquad (16)$$

and as mentioned before, the PDF of α is $f(\alpha) = \frac{1}{\pi\sigma_\alpha^2}\exp(-\frac{|\alpha|^2}{\sigma_\alpha^2})$. Consequently, the PDF of $\boldsymbol{z}$ under $\mathcal{H}_1$ conditioned on t is derived in the following theorem.

THEOREM 1 The PDF of $\boldsymbol{z}$ under $\mathcal{H}_1$ conditioned on t is

$$f(\boldsymbol{z}|\mathcal{H}_1, t) = \frac{1}{\pi^L|\boldsymbol{A}|}\frac{1}{\sigma_\alpha^2 d_t + 1}\exp\left(-\boldsymbol{z}^H\boldsymbol{A}^{-1}\boldsymbol{z}\right)$$
$$\times \exp\left(\frac{|e_t|^2\sigma_\alpha^2}{\sigma_\alpha^2 d_t + 1}\right) \qquad (17)$$

where we have defined

$$d_t = \boldsymbol{\theta}_t^H\boldsymbol{\Phi}_{(2)}^T\boldsymbol{A}^{-1}\boldsymbol{\Phi}_{(2)}\boldsymbol{\theta}_t$$
$$e_t = \boldsymbol{\theta}_t^H\boldsymbol{\Phi}_{(2)}^T\boldsymbol{A}^{-1}\boldsymbol{z}. \qquad (18)$$

PROOF The proof is derived in Appendix A.

Knowing both PDFs of $\boldsymbol{z}$ under $\mathcal{H}_0$ and $\mathcal{H}_1$ from (14) and (17), respectively, the LRT can be derived as follows:

$$L(\boldsymbol{z}|t) = \frac{f(\boldsymbol{z}|\mathcal{H}_1, t)}{f(\boldsymbol{z}|\mathcal{H}_0)} = \frac{1}{d_t\sigma_\alpha^2 + 1}\exp\left(\frac{|e_t|^2\sigma_\alpha^2}{d_t\sigma_\alpha^2 + 1}\right). \quad (19)$$

In order to find the GLRT, $L(\boldsymbol{z}|t)$ should be maximized over t

$$\text{GLRT}(\boldsymbol{z}) = \max_{t \in \{1, \ldots, L\}} L(\boldsymbol{z}|t). \qquad (20)$$

As explained in Appendix B, the GLRT can then be obtained as

$$\text{GLRT}(\boldsymbol{z}) = |e_{\hat{t}}| \gtrless \eta \qquad (21)$$

where $\hat{t} = \arg\max_{t \in \{1, \ldots, L\}} L(\boldsymbol{z}|t)$ is the estimation of the index of the target's angle cell and η is defined as the detection threshold. Since we employ the Neyman–Pearson detector [53], η is determined based on the desired false alarm probability P_{fa}.

1) *Detector Performance:* Here, we analyze the ROC of the proposed detector. It holds that

$$e_{\hat{t}}|\mathcal{H}_0 \sim \mathcal{CN}(0, d_{\hat{t}}) \qquad (22)$$

and the false alarm probability equals

$$P_{\text{fa}} = p(|e_{\hat{t}}| > \eta|\mathcal{H}_0) = \int_\eta^\infty f(x|\mathcal{H}_0)dx$$
$$= 1 - \int_{-\infty}^\eta f(x|\mathcal{H}_0)dx = \exp\left(-\frac{\eta^2}{d_{\hat{t}}}\right) \qquad (23)$$

where we introduce $x = |e_{\hat{t}}|$ and hence $x|\mathcal{H}_0 \sim$ Rayleigh(γ_0) with $\gamma_0 = (\frac{d_{\hat{t}}}{2})^{0.5}$.

Also, it holds that

$$e_{\hat{t}}|\mathcal{H}_1, \alpha \sim \mathcal{CN}(\alpha d_{\hat{t}}, d_{\hat{t}})$$
$$f(e_{\hat{t}}|\mathcal{H}_1) = \int f(e_{\hat{t}}|\mathcal{H}_1, \alpha)f(\alpha)d\alpha. \qquad (24)$$

We work out (24) in Appendix C and show that the PDF of $e_{\hat{t}}$ conditioned on $\mathcal{H}_1$ is given by

$$e_{\hat{t}}|\mathcal{H}_1 \sim \mathcal{CN}(0, d_{\hat{t}} + d_{\hat{t}}^2\sigma_\alpha^2). \qquad (25)$$

The detection probability thus equals

$$P_d = p(|e_{\hat{t}}| > \eta|\mathcal{H}_1) = \int_\eta^\infty f(x|\mathcal{H}_1)dx$$
$$= 1 - \int_{-\infty}^\eta f(x|\mathcal{H}_1)dx = \exp\left(-\frac{\eta^2}{d_{\hat{t}} + d_{\hat{t}}^2\sigma_\alpha^2}\right) \quad (26)$$

where $x|\mathcal{H}_1 \sim$ Rayleigh(γ_1) with $\gamma_1 = \left(\frac{d_{\hat{t}} + d_{\hat{t}}^2\sigma_\alpha^2}{2}\right)^{0.5}$.

Rearranging (23), it is possible to obtain η from P_{fa} as

$$\eta^2 = -d_{\hat{t}} \ln P_{\text{fa}}. \qquad (27)$$

Thus, the ROC equation is obtained as

$$P_d = \exp\left(\frac{d_{\hat{t}} \ln P_{\text{fa}}}{d_{\hat{t}} + d_{\hat{t}}^2\sigma_\alpha^2}\right) = P_{\text{fa}}^{(1 + d_{\hat{t}}\sigma_\alpha^2)^{-1}} \qquad (28)$$

where P_d is derived as a function of P_{fa}.

2) *Measurement Signal-to-Noise-and-Clutter Ratio (SNCR) at Input and Output:* In this part, we analyze the SNCR both at input and output of the detector.

For input, we need to calculate the SNCR for (7). The signal power is $\mathbb{E}\{||\alpha\boldsymbol{\psi}_t||_2^2\} = \sigma_\alpha^2 RNP$, where P is the transmit power. Also, the noise plus clutter power is $\mathbb{E}\{||\boldsymbol{\epsilon}||_2^2\} = \text{Tr}(\tilde{\boldsymbol{R}}_N)$. Therefore, the input SNCR is

$$\text{SNCR}_{\text{in}} = \frac{\sigma_\alpha^2 RNP}{\text{Tr}(\tilde{\boldsymbol{R}}_N)}. \qquad (29)$$

Based on (21), the statistic for GLRT is

$$x = |e_{\hat{t}}| = |\boldsymbol{\theta}_{\hat{t}}^H\boldsymbol{\Phi}_{(2)}^T\boldsymbol{A}^{-1}\boldsymbol{z}|. \qquad (30)$$

In Appendix D, we derive an approximation of x in the following form:

$$x = |\alpha|d_t + \Re\left\{ \frac{|\alpha|}{\alpha}\boldsymbol{\theta}_t^H \boldsymbol{\Phi}_{(2)}^T \boldsymbol{A}^{-1} \boldsymbol{\Phi}_{(2)}\boldsymbol{v} \right\}. \qquad (31)$$

Denoting α in the polar form as $\alpha = |\alpha|e^{j\omega}$, (31) can be simplified as

$$x = |\alpha|d_t + \Re\left\{ e^{-j\omega}\boldsymbol{\theta}_t^H \boldsymbol{\Phi}_{(2)}^T \boldsymbol{A}^{-1} \boldsymbol{\Phi}_{(2)}\boldsymbol{v} \right\}. \qquad (32)$$

In (32), the signal term is $|\alpha|d_t$, while the noise plus clutter term is $\Re\{e^{-j\omega}\boldsymbol{\theta}_t^H \boldsymbol{\Phi}_{(2)}^T \boldsymbol{A}^{-1} \boldsymbol{\Phi}_{(2)}\boldsymbol{v}\}$. Calculation of signal power is straightforward and is equal to $\sigma_\alpha^2 d_t^2$. For the noise and clutter term, defining $g \triangleq \boldsymbol{\theta}_t^H \boldsymbol{\Phi}_{(2)}^T \boldsymbol{A}^{-1} \boldsymbol{\Phi}_{(2)}\boldsymbol{v}$, the noise plus clutter term can be expressed as

$$\Re\left\{ e^{-j\omega}\boldsymbol{\theta}_t^H \boldsymbol{\Phi}_{(2)}^T \boldsymbol{A}^{-1} \boldsymbol{\Phi}_{(2)}\boldsymbol{v} \right\} = \Re\{ge^{-j\omega}\}$$
$$= g_r \cos\omega + g_i \sin\omega \qquad (33)$$

where g_r and g_i are the real and imaginary parts of g, respectively. Subsequently, the noise plus clutter power is given by

$$\mathbb{E}\{(g_r \cos\omega + g_i \sin\omega)^2\}$$
$$= \mathbb{E}\{g_r^2 \cos^2\omega + g_i^2 \sin^2\omega + 2g_r g_i \cos\omega \sin\omega\}$$
$$= \mathbb{E}\{g_r^2 \cos^2\omega\} \qquad (34)$$

since $\boldsymbol{v}$ is circular normal, its real and imaginary parts are statistically independent, and both are zero mean. In addition, g and ω are independent and ω has a uniform distribution in the interval $[0, 2\pi]$. Thus, noise plus clutter power P_c is calculated as follows:

$$P_c = \frac{1}{2}\mathbb{E}\{g_r^2 + g_i^2\} = \frac{1}{2}\mathbb{E}\{g^2\} = \frac{1}{2}d_t. \qquad (35)$$

As a consequence, we have

$$\text{SNCR}_{\text{out}} = 2\sigma_\alpha^2 d_t \qquad (36)$$

and using (28), the SNCR is obtained as

$$\text{SNCR}_{\text{out}} = 2\left(\frac{\ln P_{\text{fa}}}{\ln P_d} - 1\right). \qquad (37)$$

B. Multitarget Scenario

To address the multitarget scenario, we can use a deflation-type approach for detecting one target at a time, along the lines of [54]. In each iteration, using the single-target algorithm, the strongest target is extracted. If the target is greater than the threshold η, the target is detected, and its contribution is eliminated from the compressed measurement vector z. Then, iterations continue with the residual of the measurement vector, until no target is detected. The idea of residual updating is similar to the procedure done in OMP [54].

The multitarget detection algorithm proceeds as follows.

1) Initialization:

$$z_{(r)} = z$$
$$P = 0 \qquad (38)$$
$$\mathcal{A} = \varnothing.$$

2) Estimation:

$$\widehat{t}_{P+1} = \arg\max_{t \in \{1,\dots,L\}} \text{L}(z_{(r)}|t). \qquad (39)$$

3) Detection:

$$\text{GLRT}(z_{(r)}) = |e_{\widehat{t}_{P+1}}| \gtrless \eta. \qquad (40)$$

If no target is detected, terminate the algorithm.

4) Residual updating:

$$P = P + 1$$
$$\mathcal{A} = \mathcal{A} \cup \{\widehat{t}_{P+1}\}$$
$$\widehat{\boldsymbol{\alpha}} = (\boldsymbol{\Theta}[\mathcal{A}]^H \boldsymbol{\Phi}_{(2)}^T \boldsymbol{\Phi}_{(2)} \boldsymbol{\Theta}[\mathcal{A}])^\dagger \boldsymbol{\Theta}[\mathcal{A}]^H \boldsymbol{\Phi}_{(2)}^T z$$
$$z_{(r)} = z - \boldsymbol{\Phi}_{(2)} \boldsymbol{\Theta}[\mathcal{A}]\widehat{\boldsymbol{\alpha}}. \qquad (41)$$

5) Go to step 2.

Executing this multitarget detector and estimator algorithm, P is the estimated number of targets, $\mathcal{A}$ is the set of detected angle cell indices, and $\widehat{\alpha}_p$ and $\widehat{t}_p$, $p = 1, \dots, P$, are the estimated targets' amplitude and angle cell index, respectively. Subsequently, $\boldsymbol{\beta}$ is a zero vector except for the entries $\widehat{t}_p$, $p = 1, \dots, P$ which are equal to $\widehat{\alpha}_p$, $p = 1, \dots, P$.

IV. SIMULATION RESULTS

In this section, we present three sets of simulations to evaluate the proposed algorithm from different perspectives. First, the single-target case is considered, and four scenarios are simulated. The first scenario studies the effects of the number of antennas and the SNR on the performance of the proposed algorithm, while the second scenario is dedicated to the problem of grid mismatch. In the third and fourth scenarios, the proposed algorithm is compared to a state-of-the-art algorithm investigating the effect of the compression ratio and grid mismatch, respectively. The multitarget case is also considered, and the performance of the proposed approach is evaluated for different numbers of targets. Finally, a comparison between the CSP MIMO radar and the conventional CS MIMO radar in terms of saving in sample complexity is presented. Unless specifically mentioned, targets are assumed to fall on the grid.

We evaluate the performance of the proposed detection approach through an ROC analysis. We also provide the bias and standard deviation (std) of the proposed angle estimator and investigate the impact of parameters such as the number of antennas, SNR, and compression ratio, on the performance. Furthermore, we compare the proposed algorithm with one of the state-of-the-art CS recovery-based algorithms, NESTA [55], in terms of ROC, estimation accuracy, and execution time in various scenarios. NESTA is chosen, because it is a fast and accurate sparse recovery
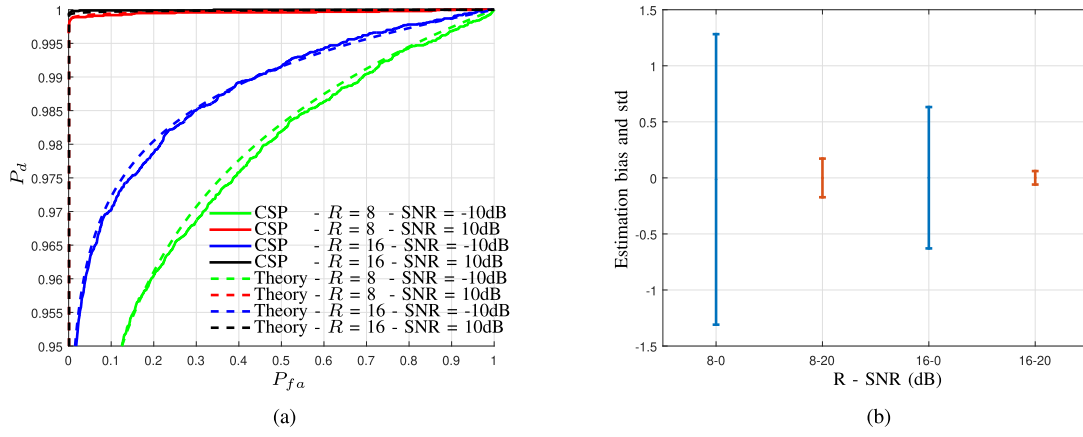
Fig. 3. Performance of the proposed CSP approach for different SNR and R values. (a) ROC. (b) Angle estimation bias and std.

TABLE I
Simulation Parameters

Description	Parameter	Value
Number of receive antennas	R	8
Number of transmit antennas	I	10
Number of samples	N	20
Signal to noise ratio	SNR	0 dB
First compression ratio	CR_1	4
Second compression ratio	CR_2	2
Clutter to noise ratio	CNR	30dB
θ span		-50 to +50 degree
θ resolution		2 degree

algorithm and is shown to perform well on the problem of signal reconstruction in the MIMO radar [3]. For the multitarget case, the OMP algorithm is also compared with the proposed algorithm. We considered the OMP algorithm for the multitarget scenario because it has a similar residual update as our proposed algorithm. It should be mentioned that the procedure for all the algorithms, i.e., CSP, NESTA, and OMP, is the same, and all are performed on z (except the last simulation), i.e., (12). A Monte Carlo simulation with 10,000 runs is employed, where unless mentioned specifically, parameters are selected based on Table I. In the following simulations, without loss of generality, the compression matrices are chosen to be Gaussian with independent identically distributed entries having zero mean and unit variance. Simulations are performed in a MATLAB R2017b environment, using an Intel Core (TM) i7-4790K, 4-GHz processor with 64 GB of memory, and under a 64-bit Microsoft Windows 10 operating system. We first present simulations for single-target scenarios and then proceed to multitarget scenarios.

A. Single-Target Scenario

Fig. 3 presents the ROC and estimation accuracy for different values of SNR and number of receive antennas, R.

In Fig. 3(a), the ROC related to the Monte Carlo simulations is plotted. The theoretical calculation in (28) is also shown, where we use the true target location t instead of $\hat{t}$. Therefore, the theoretical ROC should be an upper bound for the simulated ROC; however, it appears to match well the simulations results. In addition, increasing the SNR and R leads to a higher probability of detection for the same false alarm probability. Fig. 3(b) demonstrates the bias and std of the proposed angle estimation algorithm. Again, a reduction in estimation bias (i.e., approaching the real value) and std when increasing SNR and R is observed.

For the next scenario, we examine the performance of the proposed approach when the targets do not fall on the grid. The sensitivity of CS-based target estimation methods to grid mismatch has been extensively discussed in the literature [56]–[59]. Fig. 4 depicts the effect of both R and mismatch values on the ROC and estimation accuracy. We consider a grid mismatch equal to $0.1°$ and $1°$. It is observed from Fig. 4(a) that increasing R, improves the ROC. Although the ROC is not very sensitive to the mismatch values, an increasing mismatch results in a slightly lower probability of detection for the same false alarm probability. As demonstrated in Fig. 4(b), the proposed algorithm achieves a higher angle estimation accuracy as the number of antennas increases. In addition, it is depicted that increasing the mismatch value increases the estimation std.

As mentioned earlier, some of the important advantages of processing in the compressed domain are the reduced amounts of data, computational complexity, and memory usage in the system. Here, we compare the proposed CSP approach with one of the more recent sparse recovery methods, NESTA, from various aspects. Fig. 5 presents the comparison for different values of compression ratio CR_1. The superiority of the proposed algorithm in terms of ROC is plotted in Fig. 5(a). The theoretical calculations are also shown to be well matched with the simulation results. Moreover, as shown in Fig. 5(b), the proposed method slightly outperforms NESTA based on angle estimation accuracy.
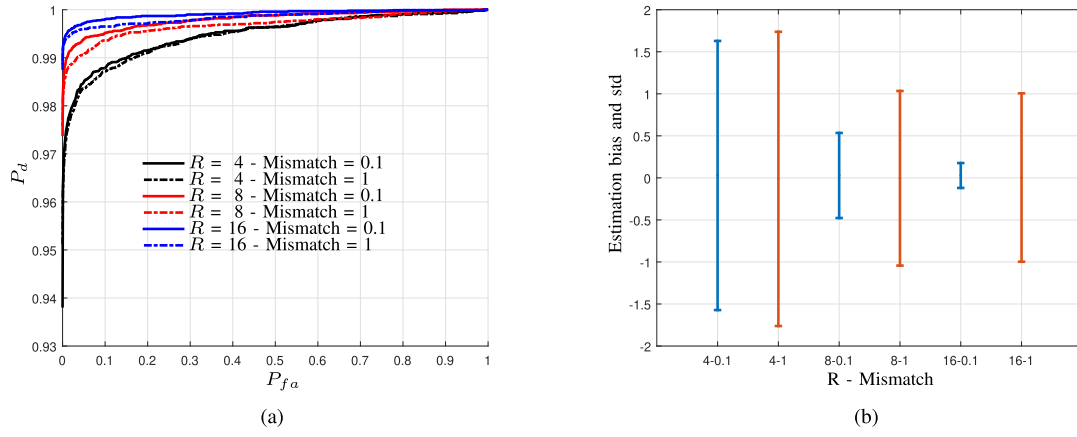
Fig. 4. Performance of the proposed CSP approach for different values of grid mismatch and R. (a) ROC. (b) Angle estimation bias and std.
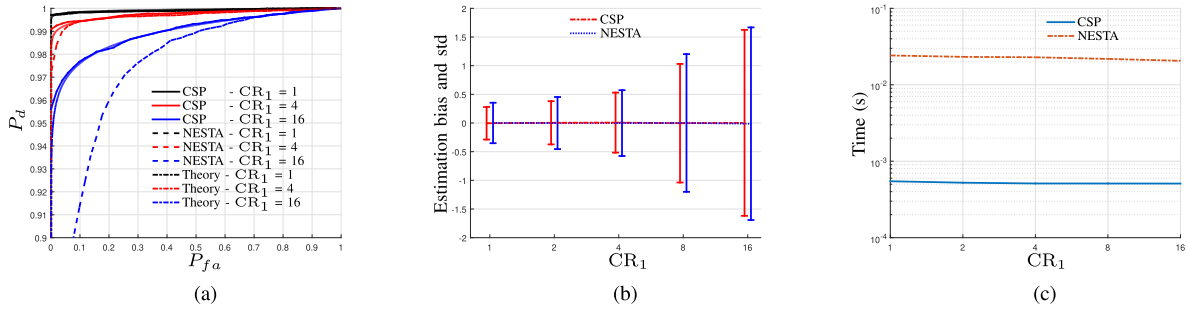

Fig. 5. Comparison of the proposed CSP approach with NESTA for different values of CR_1. (a) ROC. (b) Angle estimation bias and std. (c) Execution time.
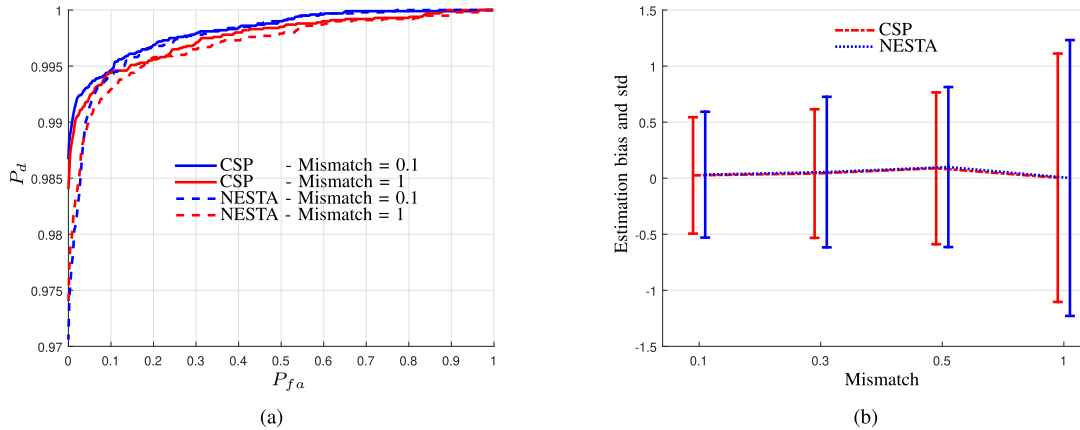

Fig. 6. Comparison of the proposed CSP approach with NESTA for different values of grid mismatch. (a) ROC. (b) Angle estimation bias and std.

Furthermore, Fig. 5(c) compares the algorithms from the execution time point of view. A significant reduction in the execution time is observed in this figure.

Fig. 6 presents a comparison with NESTA for scenarios with grid mismatch. In this case, the target grid mismatch equals $0.1°$, $0.3°$, $0.5°$, and $1°$. Although the ROC curves of both methods are close, the proposed algorithm achieves better ROC curves, which are plotted in Fig. 6(a). Also, an improved estimation accuracy of the proposed method for different values of mismatch is depicted in Fig. 6(b).

B. Multitarget Scenario

Here, we evaluate the performance of the proposed algorithm in comparison with NESTA and OMP, considering multitarget scenarios. For the following simulations, the angular cells of the targets are randomly selected with a uniform distribution. To provide a fair comparison, we assume that the number of targets Q is known for all methods. Fig. 7 depicts a sample multitarget scenario with $Q = 5$. In this figure, different amplitudes are used to improve the display. Neither the proposed CSP approach nor the NESTA and
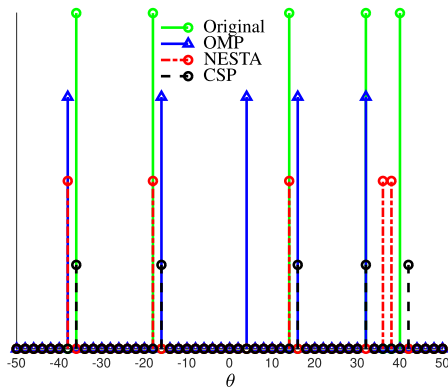
Fig. 7. Example of a multitarget scenario. Comparison of target estimation accuracy of CSP, NESTA, and OMP algorithms.

Fig. 9. Percentage of correct angle estimation versus the targets angle difference for different values of compression ratio.
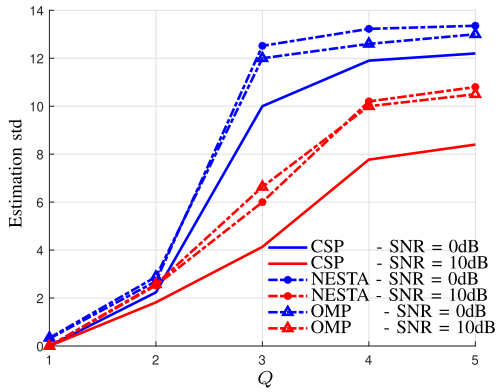

Fig. 8. Comparison of the proposed CSP approach with NESTA and OMP based on angle estimation std versus number of targets for different values of SNR.

Fig. 10. Second compression ratio CR_2 versus the first compression ratio CR_1 in order to achieve the same performance for both CSP MIMO and CS MIMO radars.

OMP algorithms find the angles exactly. Still, the proposed method provides a better estimation.

Fig. 8 presents a comparison with NESTA and OMP, where estimation std versus number of targets Q is plotted. As intuitively expected, increasing the number of targets increases the estimation std. This issue is the result of correlation among columns of the dictionary matrix Θ, which leads to an estimation error in multitarget scenarios. In other words, a linear combination of a subset of columns of Θ could be close to a linear combination of another subset of columns of Θ. This issue especially affects the performance of recovery-based algorithms. For instance, the objective of NESTA is to minimize the norm of the residual. With correlated columns of the dictionary matrix as well as noise and clutter contaminated measurements, this leads to a faulty reconstruction of the targets, since the focus is on minimizing the difference between the synthesized data vector and the measured data vector. In contrast, for the proposed CSP-based algorithm, at each step, the most likely column is selected, which leads to a smaller estimation error. Another reason for the better performance of the proposed method is the implicit whitening procedure in the procedure. Although employing the Capon beamformer, the clutter and noise power is reduced, yet the small residual effects the performance where the CSP method compensates it with
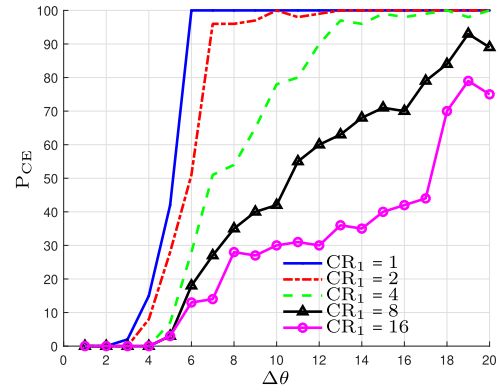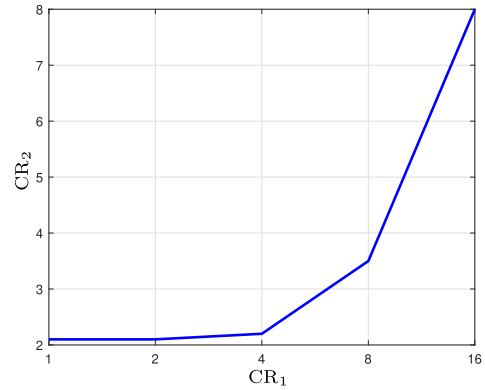
an implicit whitening filter. As shown in Fig. 8, increasing the SNR reduces the estimation error. Also, in all scenarios, the proposed approach outperforms both NESTA and OMP.

For the next simulation, we aim to observe how the proposed algorithm performs when two targets are in close angle cells and also investigate the effect of the compression ratio on its performance. Therefore, we consider a scenario with two targets and changing their angle difference, i.e., $\Delta\theta = \theta_1 - \theta_2$; we calculate the percentage of correct estimation of both angles denoted as P_{CE}. In this simulation, we assume SNR = 20 dB and $R = 20$. The rest of the parameters are similar to those in Table I. Fig. 9 presents the percentage of correct angle estimation versus the two targets angular difference for different values of the compression ratio. As expected, the estimation accuracy drops when the targets are closer. In addition, with the increase in the compression ratio, the resolvability of targets is reduced. This reduction in resolvability is due to the loss in the SNR, as the SNR is directly proportional to the number of samples. In order to prevent such an SNR loss, techniques such as compressive data acquisition directly at reception are proved to be useful [60].

C. CSP MIMO Versus CS MIMO

Here, we aim to compare the proposed CSP MIMO radar versus a conventional CS MIMO radar in terms of the number of required samples conditioned on achieving the

same performance. Considering the same first compression matrix and Capon beamformer for both approaches, the second compression matrix is only employed for the CSP MIMO radar. Moreover, the second compression ratio CR_2 is determined such that both methods achieve the same performance, i.e., estimation accuracy. For the following simulation, angle estimation accuracy is considered as the performance metric. As depicted in Fig. 10, CR_2 starting from around 2 for $CR_1 = 1$, we can increase CR_2 up to 8 for $CR_1 = 16$.

V. CONCLUSION

The MIMO radar has been receiving a lot of attention for automotive radar applications. A high data rate and computational complexity are the main drawbacks of the MIMO radar. The proposed method consists of performing temporal and spatial CS, applying the Capon beamformer to reduce the clutter, applying a second compression, and, then, formulation and solving a target detection problem on each grid of the angle space. The proposed method achieves significant sample and computational complexity and is particularly suited in applications that require low latency, such as automotive radar. Through simulations, we have illustrated that performing the signal processing in the compressed domain not only reduces sample complexity, but also improves the detection probability and angle estimation accuracy, especially in multitarget scenarios. Additionally, we have provided a mathematical analysis for the detector's ROC that was well aligned with the simulation results. As future work, we will implement the proposed algorithm over a test bed using real-world datasets in order to obtain a more realistic evaluation.

APPENDIX A
PROOF OF THEOREM 1

Using the PDF of z for hypothesis $\mathcal{H}_1$, conditioned on α and t given in (16), we prove that the PDF of z under $\mathcal{H}_1$ is

$$f(z|\mathcal{H}_1, t) = \frac{1}{\pi^L |A|} \frac{1}{\sigma_\alpha^2 d_t + 1} \exp\left(-z^H A^{-1} z\right) \times \exp\left(\frac{|e_t|^2 \sigma_\alpha^2}{\sigma_\alpha^2 d_t + 1}\right) \tag{42}$$

where d_t and e_t are defined in (18).

PROOF

$$f(z|\mathcal{H}_1, t) = \int f(z|\mathcal{H}_1, \alpha, t) f(\alpha) d\alpha$$
$$= \frac{1}{\pi^{M_2} |A|} \frac{1}{\pi \sigma_\alpha^2} \exp\left(-z^H A^{-1} z\right)$$
$$\times \int \exp\left(-\theta_t^H \Phi_{(2)}^T A^{-1} \Phi_{(2)} \theta_t |\alpha|^2\right)$$
$$\times \exp\left(\theta_t^H \Phi_{(2)}^T A^{-1} z \alpha^*\right)$$
$$\times \exp\left(z^H A^{-1} \Phi_{(2)} \theta_t \alpha\right) \exp\left(-\frac{|\alpha|^2}{\sigma_\alpha^2}\right) d\alpha. \tag{43}$$

Note that $d_t = d_t^*$ by definition. Using the definitions in (18) for d_t and e_t, (43) can be reformulated as

$$f(z|\mathcal{H}_1, t) = \frac{1}{\pi^{(M_2)} |A|} \frac{1}{\pi \sigma_\alpha^2} \exp\left(-z^H A^{-1} z\right)$$
$$\times \int \exp\left(-\left(d_t + \frac{1}{\sigma_\alpha^2}\right)|\alpha|^2\right)$$
$$\times \exp\left(e_t \alpha^* + e_t^* \alpha\right) d\alpha$$
$$= \frac{1}{\pi^{M_2} |A|} \frac{1}{\pi \sigma_\alpha^2} \exp\left(-z^H A^{-1} z\right)$$
$$\times \int \exp\left(-g_t \left(|\alpha|^2 - \frac{e_t \alpha^*}{g_t} - \frac{e_t^* \alpha}{g_t}\right)\right) d\alpha \tag{44}$$

where

$$g_t = d_t + \frac{1}{\sigma_\alpha^2}. \tag{45}$$

Thus, we have

$$f(z|\mathcal{H}_1, t) = \frac{1}{\pi^{M_2} |A|} \frac{1}{\pi \sigma_\alpha^2} \exp\left(-z^H A^{-1} z\right)$$
$$\times \int \exp\left(-g_t \left(|\alpha - \frac{e_t}{g_t}|^2 - \frac{|e_t|^2}{g_t^2}\right)\right) d\alpha$$
$$= \frac{1}{\pi^{M_2} |A|} \frac{1}{\sigma_\alpha^2 g_t} \exp\left(-z^H A^{-1} z\right) \exp\left(\frac{|e_t|^2}{g_t}\right) \tag{46}$$

which results in

$$f(z|\mathcal{H}_1, t) = \frac{1}{\pi^{M_2} |A|} \frac{1}{\sigma_\alpha^2 d_t + 1} \exp\left(-z^H A^{-1} z\right)$$
$$\times \exp\left(\frac{\sigma_\alpha^2 |e_t|^2}{\sigma_\alpha^2 d_t + 1}\right). \tag{47}$$

APPENDIX B
PROOF OF (21)

The LRT is derived as

$$L(z|t) = \frac{f(z|\mathcal{H}_1, t)}{f(z|\mathcal{H}_0)}$$
$$= \frac{1}{d_t \sigma_\alpha^2 + 1} \exp\left(\frac{|e_t|^2 \sigma_\alpha^2}{d_t \sigma_\alpha^2 + 1}\right) \gtrless \frac{p_0}{1 - p_0} \tag{48}$$

where p_0 is the *a priori* probability of the $\mathcal{H}_0$ hypothesis. It is clear that d_t is not dependent on the measurement vector, and we can simplify the LRT through the following steps:

$$L_1(z|t) = \exp\left(\frac{|e_t|^2 \sigma_\alpha^2}{d_t \sigma_\alpha^2 + 1}\right) \gtrless \frac{p_0}{1 - p_0}(d_t \sigma_\alpha^2 + 1) \tag{49}$$

and

$$L_2(z|t) = \frac{|e_t|^2 \sigma_\alpha^2}{d_t \sigma_\alpha^2 + 1} \gtrless \ln\left(\frac{p_0}{1 - p_0}(d_t \sigma_\alpha^2 + 1)\right). \tag{50}$$

As a result, we have

$$L_3(z|t) = |e_t|^2 \gtrless \frac{d_t \sigma_\alpha^2 + 1}{\sigma_\alpha^2} \ln\left(\frac{p_0}{1 - p_0}(d_t \sigma_\alpha^2 + 1)\right) \tag{51}$$

which leads to

$$L_4(z|t) = |e_t| = |\boldsymbol{\theta}_t^H \boldsymbol{\Phi}_{(2)}^T \boldsymbol{A}^{-1} z| \gtrless \eta \tag{52}$$

where we define η as the detection threshold, which is determined based on the desired false alarm probability P_{fa}.

If $L_4(z|t)$ is maximized over t, the GLRT will be $\text{GLRT}(z) = \max_{t \in \{1,\dots,L\}} L_4(z|t)$, in which $\hat{t} = \arg\max_{t \in \{1,\dots,L\}} L_4(z|t)$. Hence, the GLRT can be written as

$$\text{GLRT}(z) = L_4(z|\hat{t}) = |e_{\hat{t}}| \gtrless \eta. \tag{53}$$

APPENDIX C
PROOF OF (25)

The PDF of $e_{\hat{t}}$ conditioned on $\mathcal{H}_1$ can be computed as

$$f(e_{\hat{t}}|\mathcal{H}_1) = \int f(e_{\hat{t}}|\mathcal{H}_1,\alpha) f(\alpha) d\alpha = \frac{1}{\pi^2 d_{\hat{t}} \sigma_\alpha^2}$$

$$\times \int \exp\left(-\frac{|e_{\hat{t}} - \alpha d_{\hat{t}}|^2}{d_{\hat{t}}}\right) \exp\left(-\frac{|\alpha|^2}{\sigma_\alpha^2}\right) d\alpha$$

$$= \frac{1}{\pi^2 d_{\hat{t}} \sigma_\alpha^2} \exp\left(-\frac{|e_{\hat{t}}|^2}{d_{\hat{t}}}\right)$$

$$\times \int \exp\left(-\left(d_{\hat{t}} + \frac{1}{\sigma_\alpha^2}\right)|\alpha|^2\right)$$

$$\times \exp\left(e_{\hat{t}}^* \alpha\right) \exp\left(e_{\hat{t}} \alpha^*\right) d\alpha$$

$$= \frac{1}{\pi^2 d_{\hat{t}} \sigma_\alpha^2} \exp\left(-\frac{|e_{\hat{t}}|^2}{d_{\hat{t}}}\right)$$

$$\times \int \exp\left(-g_{\hat{t}}\left(|\alpha|^2 - \frac{e_{\hat{t}}^* \alpha}{g_{\hat{t}}} - \frac{e_{\hat{t}} \alpha^*}{g_{\hat{t}}}\right)\right) d\alpha$$

$$= \frac{1}{\pi^2 d_{\hat{t}} \sigma_\alpha^2} \exp\left(-\frac{|e_{\hat{t}}|^2}{d_{\hat{t}}}\right)$$

$$\times \int \exp\left(-g_{\hat{t}}\left(|\alpha - \frac{e_{\hat{t}}}{g_{\hat{t}}}|^2 - \frac{|e_{\hat{t}}|^2}{g_{\hat{t}}^2}\right)\right) d\alpha$$

$$= \frac{1}{\pi^2 d_{\hat{t}} \sigma_\alpha^2} \exp\left(-\frac{|e_{\hat{t}}|^2}{d_{\hat{t}}}\right) \exp\left(\frac{|e_{\hat{t}}|^2}{g_{\hat{t}}}\right)$$

$$\times \int \exp\left(-g_{\hat{t}}\left(|\alpha - \frac{e_{\hat{t}}}{g_{\hat{t}}}|^2\right)\right) d\alpha$$

$$= \frac{1}{\pi^2 d_{\hat{t}} \sigma_\alpha^2} \exp\left(-\frac{|e_{\hat{t}}|^2}{d_{\hat{t}} g_{\hat{t}} \sigma_\alpha^2}\right) \pi g_{\hat{t}}$$

$$= \frac{1}{\pi d_{\hat{t}} (d_{\hat{t}} \sigma_\alpha^2 + 1)} \exp\left(-\frac{|e_{\hat{t}}|^2}{d_{\hat{t}} (d_{\hat{t}} \sigma_\alpha^2 + 1)}\right). \tag{54}$$

APPENDIX D   PROOF OF (31)

Assuming $t = \hat{t}$, we will have

$$x = |\alpha \boldsymbol{\theta}_t^H \boldsymbol{\Phi}_{(2)}^T \boldsymbol{A}^{-1} \boldsymbol{\Phi}_{(2)} \boldsymbol{\theta}_t + \boldsymbol{\theta}_t^H \boldsymbol{\Phi}_{(2)}^T \boldsymbol{A}^{-1} \boldsymbol{\Phi}_{(2)} \boldsymbol{v}|$$

$$= |\alpha d_t + \boldsymbol{\theta}_t^H \boldsymbol{\Phi}_{(2)}^T \boldsymbol{A}^{-1} \boldsymbol{\Phi}_{(2)} \boldsymbol{v}|. \tag{55}$$

Subsequently, x^2 can be expressed as

$$x^2 = |\alpha|^2 d_t^2 + \alpha^* d_t \boldsymbol{\theta}_t^H \boldsymbol{\Phi}_{(2)}^T \boldsymbol{A}^{-1} \boldsymbol{\Phi}_{(2)} \boldsymbol{v}$$

$$+ \alpha d_t \boldsymbol{v}^H \boldsymbol{\Phi}_{(2)}^T \boldsymbol{A}^{-1} \boldsymbol{\Phi}_{(2)} \boldsymbol{\theta}_t$$

$$+ \boldsymbol{\theta}_t^H \boldsymbol{\Phi}_{(2)}^T \boldsymbol{A}^{-1} \boldsymbol{\Phi}_{(2)} \boldsymbol{v} \boldsymbol{v}^H \boldsymbol{\Phi}_{(2)}^T \boldsymbol{A}^{-1} \boldsymbol{\Phi}_{(2)} \boldsymbol{\theta}_t. \tag{56}$$

Since the Capon beamformer is applied to obtain y, we assume that $||\alpha\boldsymbol{\theta}_t||_2 \gg ||\boldsymbol{v}||$. As a consequence, x can be approximated as follows:

$$x = |\alpha| d_t \left(1 + \frac{\boldsymbol{\theta}_t^H \boldsymbol{\Phi}_{(2)}^T \boldsymbol{A}^{-1} \boldsymbol{\Phi}_{(2)} \boldsymbol{v}}{\alpha d_t} + \frac{\boldsymbol{v}^H \boldsymbol{\Phi}_{(2)}^T \boldsymbol{A}^{-1} \boldsymbol{\Phi}_{(2)} \boldsymbol{\theta}_t}{\alpha^* d_t} \right.$$

$$\left. + \frac{\boldsymbol{\theta}_t^H \boldsymbol{\Phi}_{(2)}^T \boldsymbol{A}^{-1} \boldsymbol{\Phi}_{(2)} \boldsymbol{v} \boldsymbol{v}^H \boldsymbol{\Phi}_{(2)}^T \boldsymbol{A}^{-1} \boldsymbol{\Phi}_{(2)} \boldsymbol{\theta}_t}{|\alpha|^2 d_t^2} \right)^{0.5}$$

$$\cong |\alpha| d_t \left(1 + \frac{\boldsymbol{\theta}_t^H \boldsymbol{\Phi}_{(2)}^T \boldsymbol{A}^{-1} \boldsymbol{\Phi}_{(2)} \boldsymbol{v}}{\alpha d_t} + \frac{\boldsymbol{v}^H \boldsymbol{\Phi}_{(2)}^T \boldsymbol{A}^{-1} \boldsymbol{\Phi}_{(2)} \boldsymbol{\theta}_t}{\alpha^* d_t} \right)^{0.5}$$

$$= |\alpha| d_t \left(1 + 2\Re\left\{ \frac{\boldsymbol{\theta}_t^H \boldsymbol{\Phi}_{(2)}^T \boldsymbol{A}^{-1} \boldsymbol{\Phi}_{(2)} \boldsymbol{v}}{\alpha d_t} \right\} \right)^{0.5}$$

$$\cong |\alpha| d_t \left(1 + \Re\left\{ \frac{\boldsymbol{\theta}_t^H \boldsymbol{\Phi}_{(2)}^T \boldsymbol{A}^{-1} \boldsymbol{\Phi}_{(2)} \boldsymbol{v}}{\alpha d_t} \right\} \right)$$

$$= |\alpha| d_t + \Re\left\{ \frac{|\alpha|}{\alpha} \boldsymbol{\theta}_t^H \boldsymbol{\Phi}_{(2)}^T \boldsymbol{A}^{-1} \boldsymbol{\Phi}_{(2)} \boldsymbol{v} \right\}. \tag{57}$$

REFERENCES

[1] A. M. Haimovich, R. S. Blum, and L. J. Cimini
     MIMO radar with widely separated antennas
     IEEE Signal Process. Mag., vol. 25, no. 1, pp. 116–129, Jan. 2008.

[2] M. Radmard, M. M. Chitgarha, M. N. Majd, and M. M. Nayebi
     Antenna placement and power allocation optimization in MIMO detection
     IEEE Trans. Aerosp. Electron. Syst., vol. 50, no. 2, pp. 1468–1478, Apr. 2014.

[3] E. Tohidi, M. Radmard, M. N. Majd, H. Behroozi, and M. M. Nayebi
     Compressive sensing MTI processing in distributed MIMO radars
     IET Signal Process., vol. 12, no. 3, pp. 327–334, 2017.

[4] J. Li and P. Stoica
     MIMO radar with colocated antennas
     IEEE Signal Process. Mag., vol. 24, no. 5, pp. 106–114, Sep. 2007.

[5] S. M. Karbasi, M. Radmard, M. M. Nayebi, and M. H. Bastani
     Design of multiple-input multiple-output transmit waveform and receive filter for extended target detection
     IET Radar, Sonar Navigat., vol. 9, no. 9, pp. 1345–1353, 2015.

[6] E. Tohidi, H. Behroozi, and G. Leus
     Antenna and pulse selection for colocated MIMO radar
     In *Proc. 51st Asilomar Conf. Signals, Syst., Comput.*, Oct. 2017, pp. 563–567.

[7] K. Alhujaili, V. Monga, and M. Rangaswamy
     Transmit MIMO radar beampattern design via optimization on the complex circle manifold
     IEEE Trans. Signal Process., vol. 67, no. 13, pp. 3561–3575, Jul. 2019.

[8] E. Tohidi, M. Coutino, S. P. Chepuri, H. Behroozi, M. M. Nayebi, and G. Leus
     Sparse antenna and pulse placement for colocated MIMO radar
     IEEE Trans. Signal Process., vol. 67, no. 3, pp. 579–593, Feb. 2019.

[9] M. Rossi, A. M. Haimovich, and Y. C. Eldar
     Spatial compressive sensing for MIMO radar
     IEEE Trans. Signal Process., vol. 62, no. 2, pp. 419–430, Jan. 2014.

[10] J. Ender
     On compressive sensing applied to radar
     Signal Process., vol. 90, no. 5, pp. 1402–1414, 2010.

[11] E. Tohidi, M. Radmard, S. M. Karbasi, H. Behroozi, and M. M. Nayebi
Compressive sensing in MTI processing
In *Proc. 3rd Int. Workshop Compressed Sens. Theory Appl. Radar, Sonar Remote Sens.*, Jun. 2015, pp. 189–193.

[12] F. Biondi
Compressed sensing radar-new concepts of incoherent continuous wave transmissions
In *Proc. 3rd Int. Workshop Compressed Sens. Theory Appl. Radar, Sonar Remote Sens.*, 2015, pp. 204–208.

[13] C. Larsson
Compressive sensing methods for radar cross section ISAR measurements
In *Proc. 4th Int. Workshop Compressed Sens. Theory Appl. Radar, Sonar Remote Sens.*, Sep. 2016, pp. 237–241.

[14] I. Taghavi, M. F. Sabahi, and F. Parvaresh
High resolution compressed sensing radar using difference set codes
IEEE Trans. Signal Process., vol. 67, no. 1, pp. 136–148, Jan. 2019.

[15] W. Feng, J. Friedt, G. Cherniak, and M. Sato
Batch compressive sensing for passive radar range-doppler map generation
IEEE Trans. Aerosp. Electron. Syst., vol. 55, no. 6, pp. 3090–3102, Dec. 2019.

[16] R. G. Baraniuk
Compressive sensing [lecture notes]
IEEE Signal Process. Mag., vol. 24, no. 4, pp. 118–121, Jul. 2007.

[17] E. J. Candes, J. Romberg, and T. Tao
Robust uncertainty principles: Exact signal reconstruction from highly incomplete frequency information
IEEE Trans. Inf. Theory, vol. 52, no. 2, pp. 489–509, Feb. 2006.

[18] Y. Yu, A. P. Petropulu, and H. V. Poor
MIMO radar using compressive sampling
IEEE J. Sel. Topics Signal Process., vol. 4, no. 1, pp. 146–163, 2010.

[19] I. Bilik *et al.*
Automotive MIMO radar for urban environments
In *Proc. IEEE Radar Conf.*, May 2016, pp. 1–6.

[20] S. W. Alland and J. F. Searcy
Radar system and method of digital beamforming
US Patent 7 639 171, Dec. 29, 2009.

[21] M. Wintermantel
Radar system with improved angle formation
U.S. Patent 8 665 137, Mar. 4, 2014.

[22] M. Schoor, G. Kuehnle, K. Rambach, and B. Loesch
Method for operating a MIMO radar
US Patent 9 448 302, Sep. 20, 2016.

[23] D. Cohen, D. Cohen, Y. C. Eldar, and A. M. Haimovich
SUMMeR: Sub-Nyquist MIMO radar
IEEE Trans. Signal Process., vol. 66, no. 16, pp. 4315–4330, Aug. 2018.

[24] P. Chen, C. Qi, L. Wu, and X. Wang
Estimation of extended targets based on compressed sensing in cognitive radar system
IEEE Trans. Veh. Technol., vol. 66, no. 2, pp. 941–951, Feb. 2017.

[25] S. Gogineni and A. Nehorai
Target estimation using sparse modeling for distributed MIMO radar
IEEE Trans. Signal Process., vol. 59, no. 11, pp. 5315–5325, Nov. 2011.

[26] B. Li and A. P. Petropulu
Distributed MIMO radar based on sparse sensing: Analysis and efficient implementation
IEEE Trans. Aerosp. Electron. Syst., vol. 51, no. 4, pp. 3055–3070, Oct. 2015.

[27] M. A. Herman and T. Strohmer
High-resolution radar via compressed sensing
IEEE Trans. Signal Process., vol. 57, no. 6, pp. 2275–2284, Jun. 2009.

[28] Y. Yu, S. Sun, R. N. Madan, and A. Petropulu
Power allocation and waveform design for the compressive sensing based MIMO radar
IEEE Trans. Aerosp. Electron. Syst., vol. 50, no. 2, pp. 898–909, Apr. 2014.

[29] L. Lei, J. Huang, and Y. Sun
Compressed sensing MIMO radar waveform optimization without signal recovery
In *Proc. CIE Int. Conf. Radar*, 2016, pp. 1–4.

[30] A. Ajorloo, A. Amini, and M. H. Bastani
A compressive sensing-based colocated MIMO radar power allocation and waveform design
IEEE Sens. J., vol. 18, no. 22, pp. 9420–9429, Nov. 2018.

[31] S. Salari, F. Chan, Y. Chan, I. Kim, and R. Cormier
Joint DOA and clutter covariance matrix estimation in compressive sensing MIMO radar
IEEE Trans. Aerosp. Electron. Syst., vol. 55, no. 1, pp. 318–331, Feb. 2019.

[32] D. Needell and J. A. Tropp
CoSaMP: Iterative signal recovery from incomplete and inaccurate samples
Appl. Comput. Harmonic Anal., vol. 26, no. 3, pp. 301–321, 2009.

[33] T. Huang, Y. Liu, and X. Wang
Adaptive subspace pursuit and its application in motion compensation for step frequency radar
In *1st Int. Workshop Compressed Sens. Appl. Radar*, 2012.

[34] B. Zhang, X. Cheng, N. Zhang, Y. Cui, Y. Li, and Q. Liang
Sparse target counting and localization in sensor networks based on compressive sensing
In *Proc. IEEE INFOCOM*, Apr. 2011, pp. 2255–2263.

[35] M. A. Davenport, P. T. Boufounos, M. B. Wakin, and R. G. Baraniuk
Signal processing with compressive measurements
IEEE J. Sel. Topics Signal Process., vol. 4, no. 2, pp. 445–460, Apr. 2010.

[36] A. Hariri and M. Babaie-Zadeh
Compressive detection of sparse signals in additive white gaussian noise without signal reconstruction
Signal Process., vol. 131, pp. 376–385, 2017.

[37] S. Gishkori, V. Lottici, and G. Leus
Compressive sampling-based multiple symbol differential detection for UWB communications
IEEE Trans. Wireless Commun., vol. 13, no. 7, pp. 3778–3790, Jul. 2014.

[38] A. Hariri and M. Babaie-Zadeh
Joint compressive single target detection and parameter estimation in radar without signal reconstruction
IET Radar, Sonar Navigat., vol. 9, no. 8, pp. 948–955, 2015.

[39] M. C. Wicks, H. Kung, and H.-C. Chen
Compressed statistical testing and application to radar
1st Int. Workshop Compressed Sens. Appl. Radar, Bonn, Germany, 14–16 May, 2012.

[40] C. W. Lim and M. B. Wakin
Automatic modulation recognition for spectrum sensing using nonuniform compressive samples
In *Proc. IEEE Int. Conf. Commun.*, Jun. 2012, pp. 3505–3510.

[41] C. W. Lim and M. B. Wakin
CHOCS: A framework for estimating compressive higher order cyclostationary statistics
Proc. SPIE, vol. 8365, 2012, Art. no. 83650M.

[42] Y. Wang, A. Pandharipande, and G. Leus
Compressive sampling based MVDR spectrum sensing
In *Proc. 2nd Int. Workshop Cogn. Inf. Process.*, Jun. 2010, pp. 333–337.

[43] M. Skolnik
Introduction to Radar Systems (ser. Electrical engineering series). New York, NY, USA: McGraw-Hill, 2001.

[44] V. Kovalenko, A. G. Yarovoy, and L. P. Ligthart
A novel clutter suppression algorithm for landmine detection with GPR
IEEE Geosci. Remote Sens. Lett., vol. 45, no. 11, pp. 3740–3751, Oct. 2007.

[45] X. Meng, T. Wang, J. Wu, and Z. Bao
Short-range clutter suppression for airborne radar by utilizing prefiltering in elevation
IEEE Geosci. Remote Sens. Lett., vol. 6, no. 2, pp. 268–272, Apr. 2009.

[46] T. K. Sjgren *et al.*
Suppression of clutter in multichannel SAR GMTI
IEEE Trans. Geosci. Remote Sens., vol. 52, no. 7, pp. 4005–4013, Jul. 2014.

[47] B. Tang and J. Tang
Joint design of transmit waveforms and receive filters for MIMO radar space-time adaptive processing
IEEE Trans. Signal Process., vol. 64, no. 18, pp. 4707–4722, Sep. 2016.

[48] Y. Yu, S. Sun, and A. P. Petropulu
A Capon beamforming method for clutter suppression in colocated compressive sensing based MIMO radars
Proc. SPIE, vol. 8717, 2013, Art. no. 87170J.

[49] D. S. Kalogerias and A. P. Petropulu
Matrix completion in colocated MIMO radar: Recoverability, bounds theoretical guarantees
IEEE Trans. Signal Process., vol. 62, no. 2, pp. 309–321, Jan. 2014.

[50] S. Sun, W. U. Bajwa, and A. P. Petropulu
MIMO-MC radar: A MIMO radar approach based on matrix completion
IEEE Trans. Aerosp. Electron. Syst., vol. 51, no. 3, pp. 1839–1852, Jul. 2015.

[51] H. L. Van Trees
Optimum Array Processing: Part IV of Detection, Estimation and Modulation Theory, vol. 1. Hoboken, NJ, USA: Wiley Online Library, 2002.

[52] A. Papoulis and S. U. Pillai
Probability, Random Variables, and Stochastic Processes. Noida, India: Tata McGraw-Hill Education, 2002.

[53] H. V. Poor
An Introduction to Signal Detection and Estimation. New York, NY, USA: Springer, 2013.

[54] J. A. Tropp and A. C. Gilbert
Signal recovery from random measurements via orthogonal matching pursuit
IEEE Trans. Inf. Theory, vol. 53, no. 12, pp. 4655–4666, Dec. 2007.

[55] S. Becker, J. Bobin, and E. J. Candès
NESTA: A fast and accurate first-order method for sparse recovery
SIAM J. Imag. Sci., vol. 4, no. 1, pp. 1–39, 2011.

[56] Y. Chi, L. L. Scharf, A. Pezeshki, and A. R. Calderbank
Sensitivity to basis mismatch in compressed sensing
IEEE Trans. Signal Process., vol. 59, no. 5, pp. 2182–2195, May 2011.

[57] G. Tang, B. N. Bhaskar, P. Shah, and B. Recht
Compressed sensing off the grid
IEEE Trans. Inf. Theory, vol. 59, no. 11, pp. 7465–7490, Nov. 2013.

[58] Z. Yang, L. Xie, and C. Zhang
Off-grid direction of arrival estimation using sparse Bayesian inference
IEEE Trans. Signal Process., vol. 61, no. 1, pp. 38–43, Jan. 2013.

[59] H. Zhu, G. Leus, and G. B. Giannakis
Sparsity-cognizant total least-squares for perturbed compressive sampling
IEEE Trans. Signal Process., vol. 59, no. 5, pp. 2002–2016, May 2011.

[60] R. Pribi, G. Leus, and C. Tzotzadinis
Signal-to-noise-ratio analysis of compressive data acquisition
In *Proc. IEEE Statist. Signal Process. Workshop*, 2018, pp. 603–607.

Ehsan Tohidi (Member, IEEE) received the B.Sc., M.Sc., and Ph.D. degrees in electrical engineering (with a specialization on communications and signal processing) from the Sharif University of Technology, Tehran, Iran, in 2011, 2013, and 2018, respectively.

From September 2016 to March 2017, he was a Visiting Ph.D. Student with the Department of Electrical Engineering, Mathematics, and Computer Science, Delft University of Technology, Delft, The Netherlands. He is currently a Postdoctoral Researcher with Eurecom, Biot, France. His research interests include signal processing, discrete and continuous optimization, resource allocation, and machine learning.

Alireza Hariri received the B.Sc., M.Sc., and Ph.D. degrees in electrical engineering from the Sharif University of Technology, Tehran, Iran, in 2007, 2009, and 2017, respectively.

Hamid Behroozi (Member, IEEE) received the B.Sc. degree from the University of Tehran, Tehran, Iran, in 2000, the M.Sc. degree from the Sharif University of Technology, Tehran, in 2003, and the Ph.D. degree from Concordia University, Montreal, QC, Canada, in 2007, all in electrical engineering.

From 2007 to 2010, he was a Postdoctoral Fellow with the Department of Mathematics and Statistics, Queen's University, Kingston, ON, Canada. He is currently an Associate Professor with the Department of Electrical Engineering, Sharif University of Technology. His research interests include information theory, joint source-channel coding, artificial intelligence in signal processing and data science, and cooperative communications.

Dr. Behroozi was a recipient of several academic awards, including the Ontario Postdoctoral Fellowship awarded by the Ontario Ministry of Research and Innovation, the Quebec Doctoral Research Scholarship awarded by the Government of Quebec (FQRNT), the Hydro Quebec Graduate Award, and the Concordia University Graduate Fellowship.

Mohammad Mahdi Nayebi (Senior Member, IEEE) received the B.S. and M.S. degrees in analysis and design of nonuniformly sampled digital filters for application in moving target indication radars from the Sharif University of Technology, Tehran, Iran, in 1988 and 1990, respectively, and the Ph.D. degree in electrical engineering (with a specialization on detection of radar targets in clutter plus noise) from Tarbiat Modares University, Tehran, in 1994.

In 1994, he joined the Sharif University of Technology, where he is working on multiple-input multiple-output radar signal processing. His main research interests include detection and estimation theory, radar signal processing, pattern recognition, electromagnetic compatibility, and communications.

Geert Leus (Fellow, IEEE) received the M.Sc. and Ph.D. degrees in electrical engineering from Katholieke Universiteit Leuven, Leuven, Belgium, in 1996 and 2000, respectively.

He is currently an "Antoni van Leeuwenhoek" Full Professor with the Faculty of Electrical Engineering, Mathematics and Computer Science, Delft University of Technology, Delft, The Netherlands. His research interests include the broad area of signal processing, with a specific focus on wireless communications, array processing, sensor networks, and graph signal processing.

Dr. Leus received the 2002 IEEE Signal Processing Society Young Author Best Paper Award and the 2005 IEEE Signal Processing Society Best Paper Award. He is a fellow of the European Association for Signal Processing (EURASIP). He was a Member-at-Large of the Board of Governors of the IEEE Signal Processing Society, the Chair of the IEEE Signal Processing for Communications and Networking Technical Committee, a member of the IEEE Sensor Array and Multichannel Technical Committee, a member of the IEEE Big Data Special Interest Group, and the Editor-in-Chief of the *EURASIP Journal on Advances in Signal Processing*. He was also on the Editorial Boards of the IEEE TRANSACTIONS ON SIGNAL PROCESSING, the IEEE TRANSACTIONS ON WIRELESS COMMUNICATIONS, the IEEE SIGNAL PROCESSING LETTERS, and the *EURASIP Journal on Advances in Signal Processing*. He is the Chair of the EURASIP Technical Area Committee on Signal Processing for Multisensor Systems, a member of the IEEE Signal Processing Theory and Methods Technical Committee, an Associate Editor for the *Foundations and Trends in Signal Processing*, and the Editor-in-Chief of *EURASIP Signal Processing*.

Athina P. Petropulu (Fellow, IEEE) received the M.Sc. and Ph.D. degrees in electrical and computer engineering from Northeastern University, Boston MA, in 1988 and 1991, respectively. She is a Distinguished Professor with the Department of Electrical and Computer Engineering (ECE), Rutgers—The State University of New Jersey, where she was the Chair of the Department from 2010 to 2016. Prior to joining Rutgers, she was a Professor of ECE with Drexel University from 1992 to 2010. She held Visiting Scholar appointments with SUPELEC, Universite Paris Sud, Princeton University, and University of Southern California. Her research interests include statistical signal processing, wireless communications, signal processing in networking, physical layer security, and radar signal processing. Her research has been funded by various government industry sponsors, including the National Science Foundation (NSF), the Office of Naval research, the U.S. Army, the National Institute of Health, the Whitaker Foundation, Lockheed Martin, and Raytheon.

Dr. Petropulu is the recipient of the 1995 Presidential Faculty Fellow Award given by the NSF and the White House. She is President-Elect for the IEEE Signal Processing Society for 2020–2021, and in the past, she has served as the Editor-in-Chief of the IEEE TRANSACTIONS ON SIGNAL PROCESSING, from 2009 to 2011, and IEEE Signal Processing Society Vice President—Conferences, from 2006 to 2008. She was the General Chair of the 2005 International Conference on Acoustics Speech and Signal Processing, Philadelphia PA, USA, and is the General Co-Chair of the 2018 IEEE International Workshop on Signal Processing Advances in Wireless Communications. She is also the recipient of the 2005 IEEE Signal Processing Magazine Best Paper Award and the 2012 IEEE Signal Processing Society Meritorious Service Award. She was a Distinguished Lecturer for the IEEE Signal Processing Society from 2017 to 2018. She is a currently Distinguished Lecturer for the IEEE Aerospace and Electronics Systems Society. She is also a fellow of the American Association for the Advancement of Science.